

# Machine Learning-Based Classification of Jhana Advanced Concentrative Absorption Meditation (ACAM-J) using 7T fMRI

Puneet Kumar<sup>1</sup>, Winson F.Z. Yang<sup>2,3</sup>, Alakhsimar Singh<sup>4</sup>, Xiaobai Li<sup>5</sup>, Matthew D. Sacchet<sup>2,3\*</sup>

## Affiliations

<sup>1</sup>School of AI and Data Engineering, Indian Institute of Technology Ropar 140001, India

<sup>2</sup>Meditation Research Program, Department of Psychiatry, Massachusetts General Hospital, Harvard Medical School, Boston, MA 02129, USA

<sup>3</sup>Athinoula A. Martinos Center for Biomedical Imaging, Department of Radiology, Massachusetts General Hospital, Harvard Medical School, Boston, MA 02129, USA

<sup>4</sup>Computer Science and Engineering Department, National Institute of Technology Jalandhar 144008, India

<sup>5</sup>State Key Laboratory of Blockchain and Data Security, Zhejiang University, Hangzhou, 310027, China.

## \*Corresponding author:

Meditation Research Program, Department of Psychiatry, Massachusetts General Hospital, Harvard Medical School, Boston, MA 02129, USA.

Email: [meditationadministration@mgh.harvard.edu](mailto:meditationadministration@mgh.harvard.edu)

## Abstract

Jhana advanced concentration absorption meditation (ACAM-J) is related to profound changes in consciousness and cognitive processing, making the study of their neural correlates vital for insights into consciousness and well-being. This study evaluates whether functional MRI-derived regional homogeneity (ReHo) can be used to classify ACAM-J using machine-learning approaches. We collected group-level fMRI data from 20 advanced meditators to train the classifiers, and intensive single-case data from an advanced practitioner performing ACAM-J and control tasks to evaluate generalization. ReHo maps were computed, and features were extracted from predefined brain regions of interest. We trained multiple machine learning classifiers using stratified cross-validation to evaluate whether ReHo patterns distinguish ACAM-J from non-meditative states. Ensemble models achieved 66.82% ( $p < 0.05$ ) accuracy in

distinguishing ACAM-J from control conditions. Feature-importance analysis indicated that prefrontal and anterior cingulate areas contributed most to model decisions, aligning with established involvement of these regions in attentional regulation and metacognitive processes. Moreover, moderate agreement reflected in Cohen's  $\kappa$  supports the feasibility of using machine learning to distinguish ACAM-J from non-meditative states. These findings advocate machine-learning's feasibility in classifying advanced meditation states, future research on neuromodulation and mechanistic models of advanced meditation.

**Keywords:** Advanced meditation, advanced concentration absorption meditation-jhana type (ACAM-J), neurophenomenology, machine learning, 7T functional magnetic resonance imaging (fMRI), regional homogeneity.

## 1. Introduction

With advanced meditation training, human consciousness can reorganize into highly structured, non-ordinary modes of awareness<sup>1</sup>. One such training in which contemplative traditions describe involves deep absorption where attention becomes stable, sensory processes and inner narration diminishes, and experiences of inner joy develops. Unlike the heterogeneous effects of more basic forms of meditation<sup>2,3</sup>, these advanced meditation states are structured, reproducible, and with distinct and reportable phenomenology<sup>4-9</sup>. These experiences remain almost entirely unstudied in modern science, despite their significance in contemplative traditions<sup>10</sup>. Here, we view these states as alternate attentional configurations that provide a complementary reference point for studying peak human experiences, sustained attention, equanimity, and well-being<sup>1,11,12</sup>.

Among the most systematically described and replicable frameworks for advanced meditation in contemplative traditions is jhana, a sequence of eight absorption states preserved in Buddhism for over two thousand years<sup>13-15</sup>. In this work, we refer to the practice in scientific terms as jhana advanced concentration absorption meditation (ACAM-J) to differentiate the neurocognitive phenomena under study from doctrinal or interpretive accounts<sup>10</sup>. This terminology allows a precise scientific treatment grounded in first-person phenomenology while avoiding long-standing definitional debates surrounding jhana.

ACAM-J comprises eight progressive states of advanced meditation that unfold through increasingly refined absorption and attentional stability<sup>12</sup>. Early ACAM-J are marked by pronounced positive affect, including feelings of joy, bliss, and energized yet stable attention. In contrast, later ACAM-J are characterized by a profound sense of formlessness, accompanied by diminished sensory content and reduced self-referential thought. Awareness in these stages becomes expansive, boundless, and subtle, often described as a spacious void or a mode of consciousness that

transcends ordinary perception. Each ACAM-J is phenomenologically distinct and can be reliably reported by experienced practitioners<sup>7</sup>. Despite its scientific importance to the science of consciousness and clinical potential<sup>10,16,17</sup>, systematic neuroscientific investigation of ACAM-J remains limited.

Recent neuroscientific investigations of ACAM-J have mapped its neural dynamics using high-resolution EEG and fMRI, revealing distinct brain states associated with concentrative absorption<sup>18–20</sup>. However, these studies rely on univariate analyses, which can detect group-level differences but not the high-dimensional “neural fingerprint” distinguishing brain states that machine learning (ML) offers<sup>21</sup>. ML applications to standard meditation practices have uncovered insights into neural mechanisms and associated cognitive changes<sup>22,23</sup>. Extending these approaches to advanced meditation would allow high-resolution tracking of neural dynamics during absorption, support the discovery of physiological markers that correlate with meditative depth and clinical outcomes, and provide data-driven criteria for distinguishing ACAM-J<sup>5,17,23,24</sup>.

In this study, we introduce an integrated computational framework that combines ensemble learning, data-balancing strategies, and rigorous evaluation procedures to classify ACAM-J. We implemented the Synthetic Minority Over-sampling Technique (SMOTE) with repeated stratified cross-validation to ensure consistent class distributions across folds and maintaining data integrity. This approach ensured that each fold of our data maintained a consistent distribution of classes, which is vital for preserving data integrity throughout the training process and achieving stable, reliable performance metrics. Six ML models, logistic regression, decision trees, random forest, support vector machines with linear kernels, *k*-nearest neighbors, and artificial neural networks, were trained, and the top three performers were combined through ensemble averaging to enhance predictive accuracy. The resulting binary classification between ACAM-J and control conditions achieved an accuracy of 66.82%, demonstrating the promise of computational methods for characterizing advanced meditative states. Feature-importance analyses further highlighted key brain regions contributing to classification, offering insights into the neural mechanisms supporting deep absorption. Together, these methods establish a scalable analytical framework for the multivariate study of ACAM-J, illustrating how ML can deepen empirical understanding of advanced meditation and providing a foundation for future contemplative neuroscience and therapeutic applications.

## 2. Results

### ACAM-J vs control conditions

We first evaluated the broad distinction between ACAM-J and non-ACAM-J. ReHo differences between these categories reveal distinct functional signatures, with the most discriminative regions spanning the default mode

network (medial prefrontal and posterior parietal cortices), anterior insula, anterior cingulate cortex, and the locus coeruleus (**Fig. 1**). Using machine-learning classifiers, the model achieved an accuracy of 73.19% and a Cohen's kappa ( $\kappa$ ) of 0.2604, reflecting performance moderately above chance ( $p < 0.05$ ) in differentiating the two global states.

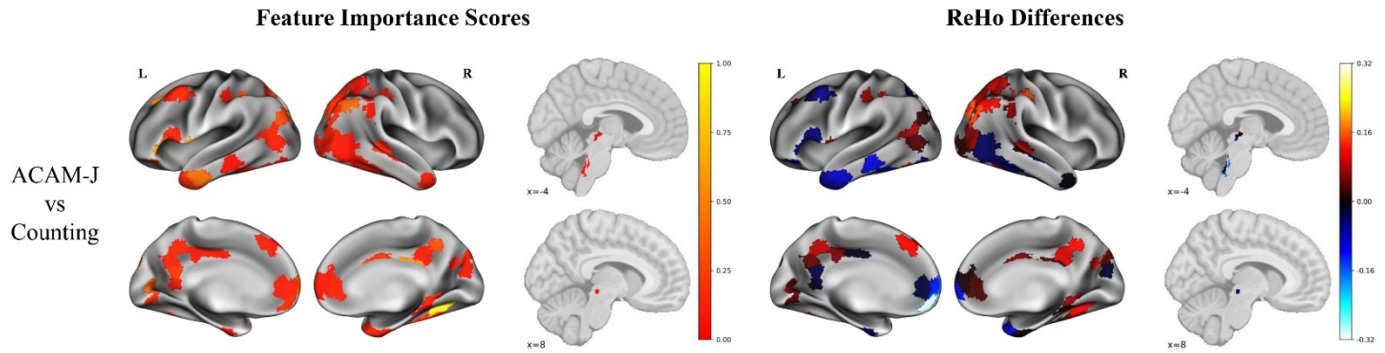


**Fig. 1: Brain-plots for ACAM-J vs control conditions.** Left panels denote feature-significant analysis highlighting the cortical and subcortical analysis of the ROIs identified via the pairwise feature significance analysis, with the color bar indicating normalized feature-importance scores. Right panels show whole-brain surface maps of the average ReHo difference between all ACAM-J and combined control (counting + memory) conditions, with the color bar indicating ReHo differences, with warm colors indicating higher ReHo during ACAM-J and cool colors the opposite.

Next, we examined the contrast between ACAM-J and the counting task. As shown in Fig. 2, ReHo differences reveal distinct spatial patterns across the six ACAM-J stages relative to counting. Discriminative regions include the locus coeruleus, as well as distributed clusters across visual, control, default mode, and salience networks. Beginning with ACAM-J4, regions within the dorsal attention network become increasingly prominent, suggesting a shift toward more stable and sustained attentional engagement during mid-to-late ACAM-J. Classification performance reached an accuracy of 66.31% with a Cohen's  $\kappa = 0.2615$ , indicating moderate discriminability but slightly reduced performance relative to the broader ACAM-J vs. non-ACAM-J comparison. Detailed metrics for each ACAM-J stage, including accuracy,  $\kappa$ , AUC, precision, recall, F1 score, sensitivity, specificity, and  $p$ -values, are summarized in Table 1.

**Table 1:** Classification metrics for ACAM-J vs. Counting Task. The accuracy (Acc), Cohen's kappa (CK), Area under the ROC curve (AUC), Precision, Recall/Sensitivity, F1 (harmonic mean of precision and recall), Specificity (TNR) and p- value are reported, quantifying the discriminability.

Metric	ACAM-J vs	ACAM-J1 vs	ACAM-J2 vs	ACAM-J3 vs	ACAM-J4 vs	ACAM-J5 vs	ACAM-J6 vs
	Counting	Counting	Counting	Counting	Counting	Counting	Counting
<b>Acc</b>	0.7319	0.7044	0.6524	0.7150	0.5363	0.7086	0.6618
<b>CK</b>	0.2604	0.2882	0.2609	0.2739	0.0875	0.3306	0.3278
<b>AUC</b>	0.7892	0.7536	0.6903	0.7693	0.5313	0.7616	0.7027
<b>Precision</b>	0.7415	0.7213	0.6689	0.7346	0.5447	0.7298	0.6821
<b>Recall / Sens.</b>	0.7368	0.7142	0.6613	0.7284	0.5412	0.7244	0.6765
<b>F1</b>	0.7396	0.7177	0.6651	0.7315	0.5429	0.7271	0.6793
<b>Specificity</b>	0.6270	0.6946	0.6435	0.7016	0.5314	0.6928	0.6471
<b>p-Value</b>	<0.001	<0.001	<0.001	<0.001	<0.001	<0.001	0.029

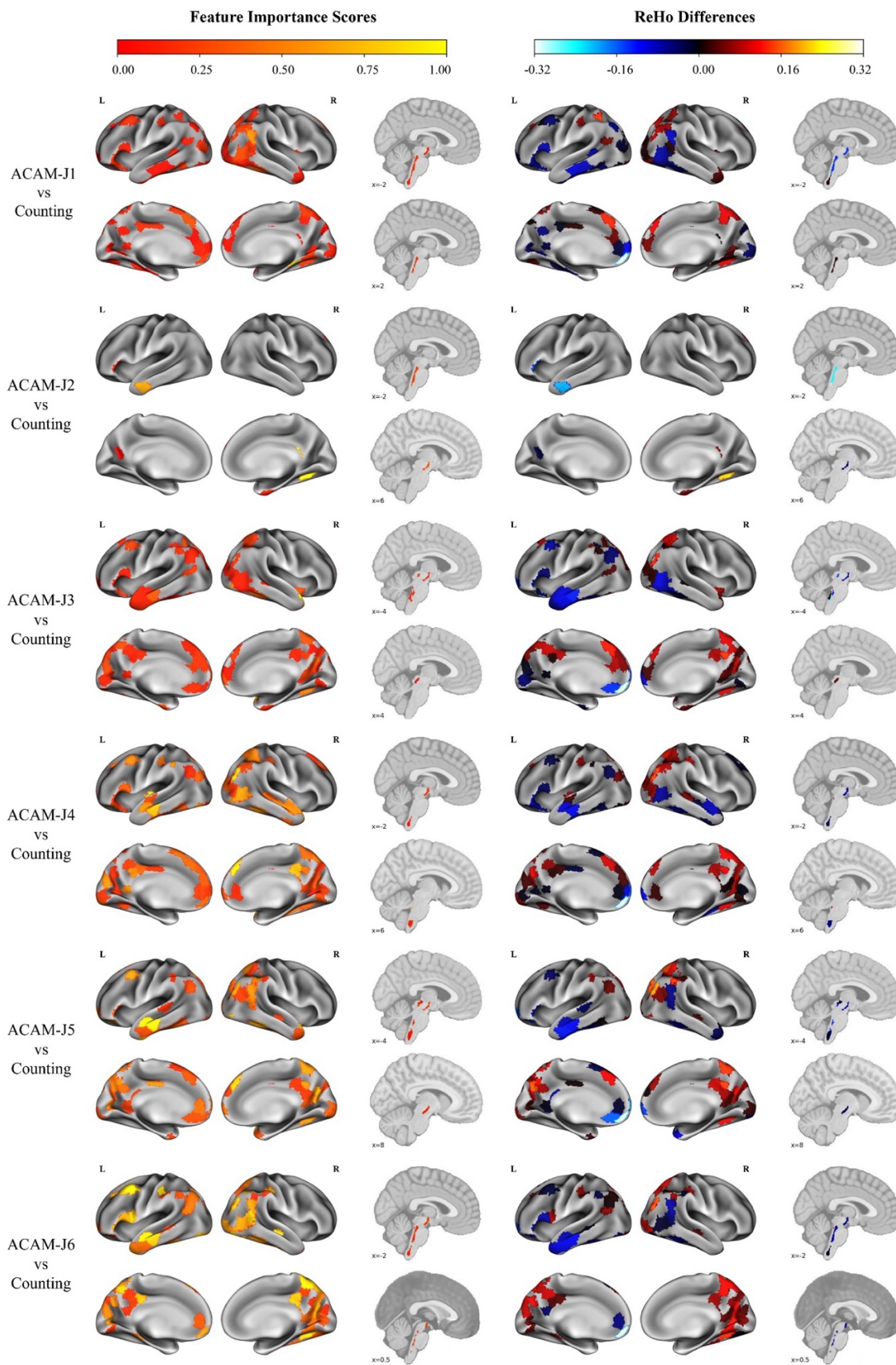


**Fig. 2: Brain-plots for ACAM-J vs. counting.** Left panels denote feature-significant analysis highlighting the cortical and subcortical ROIs identified via the pairwise feature significance analysis, with the color bar indicating normalized feature-importance scores. Right panels show six sagittal slices of the average ReHo difference for each comparison, with the color bar indicating ReHo differences, with warm colors indicating higher local synchronization during ACAM-J and cool colors the opposite.

When distinguishing ACAM-J from the memory task, the model achieved an accuracy of 63.94% and a Cohen's  $\kappa$  of 0.1908, indicating modest but meaningful discriminability. The brain plots and detailed performance metrics for each ACAM-J stage relative to memory are provided in **Fig. 3** and **Table 2** respectively. ACAM-J exhibits increased ReHo within default mode and control networks, as well as salience network regions and the locus coeruleus. These regions become especially prominent in ACAM-J5 and ACAM-J6. Interestingly, unexpected neural signatures were observed particularly for J2 versus counting and memory, highlighting potential neurophenomenological distinctions warranting further exploration in the discussion.

**Table 2:** Classification metrics for ACAM-J vs. Memory. The accuracy (Acc), Cohen's kappa (CK), Area under the ROC curve (AUC), Precision, Recall/Sensitivity, F1 (harmonic mean of precision and recall), Specificity (TNR) and *p*-value are reported, quantifying the discriminability.

Metric	ACAM-J1 vs	ACAM-J2 vs	ACAM-J3 vs	ACAM-J4 vs	ACAM-J5 vs	ACAM-J6 vs
	Memory	Memory	Memory	Memory	Memory	Memory
<b>Acc</b>	0.6475	0.5824	0.7034	0.4937	0.6667	0.7430
<b>CK</b>	0.1928	0.1329	0.2406	0.1102	0.1521	0.3164
<b>AUC</b>	0.6743	0.5959	0.7460	0.5011	0.6993	0.7937
<b>Precision</b>	0.6629	0.5946	0.7215	0.5047	0.6799	0.7653
<b>Recall / Sens.</b>	0.6749	0.6045	0.7353	0.5137	0.6905	0.7818
<b>F1</b>	0.6689	0.5995	0.7283	0.5091	0.6852	0.7734
<b>Specificity</b>	0.6199	0.5603	0.6715	0.4737	0.6429	0.7042
<b>p-Value</b>	<0.001	<0.001	<0.001	<0.001	<0.001	<0.001

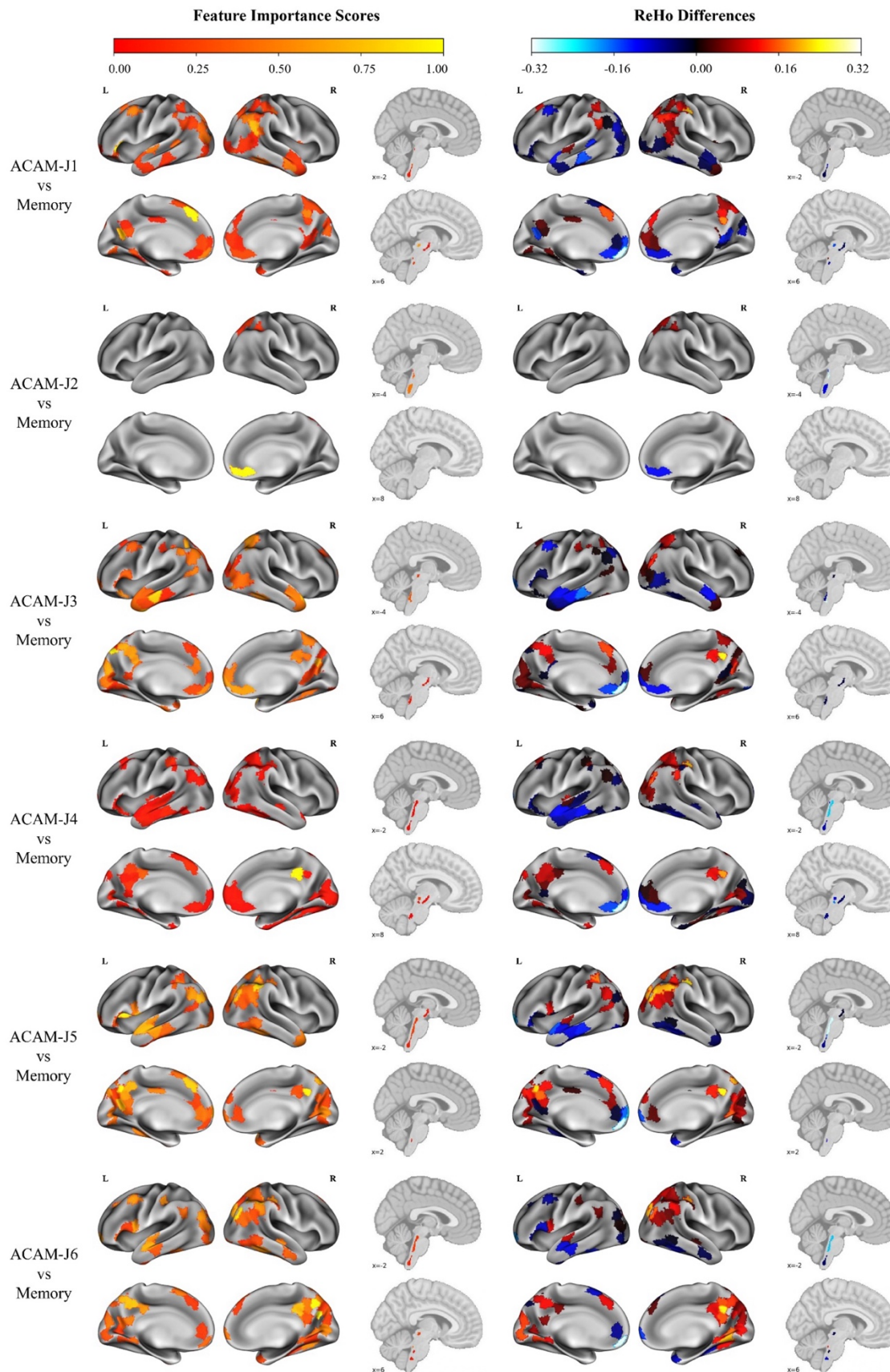


**Fig. 3: Brain-plots for ACAM-J vs. Memory task.** Left panels denote feature-significant analysis highlighting the cortical and subcortical ROIs identified via the pairwise feature significance analysis, with the color bar indicating normalized feature-importance scores. Right panels show axial and coronal slices of the average ReHo difference between each comparison, with the color bar indicating ReHo differences, with warm colors marking increased synchronization in ACAM-J. Only ROIs selected by permutation-based significance across all folds are displayed, emphasizing consistent discriminators within default-mode, control, salience networks, and the locus coeruleus (see Table 2 for evaluation metrics).

## Pairwise ACAM-J classification

Pairwise classification between adjacent ACAM-J stages provides a finer-grained view of neurophenomenological transitions (**Table 3; Fig. 4**). Across all ACAM-J pairs, the model achieved an overall accuracy of 64.22% with a Cohen's  $\kappa$  of 0.1822, indicating modest but meaningful discriminability among closely related states. ReHo contrasts reveal progressive shifts in ReHo associated with ACAM-J depth. Key discriminative regions include hubs of the default mode network, particularly medial prefrontal areas, along with the cingulate, control network nodes, salience network regions, and locus coeruleus. These regions become especially prominent from ACAM-J4 onward.

**Table 3:** Classification metrics for successive ACAM-J pairs and ACAM-J1 vs ACAM-J6. The accuracy (Acc), Cohen's kappa (CK), Area under the ROC curve (AUC), Precision, Recall/Sensitivity, F1 (harmonic mean of precision and recall), Specificity (TNR) and p- value are reported, quantifying the discriminability.

Metric	ACAM-J1 vs ACAM-J2		ACAM-J2 vs ACAM-J3		ACAM-J3 vs ACAM-J4		ACAM-J4 vs ACAM-J5		ACAM-J5 vs ACAM-J6		ACAM-J1 vs ACAM-J6	
	ACAM-J2	ACAM-J3	ACAM-J4	ACAM-J5	ACAM-J6	ACAM-J6	ACAM-J6	ACAM-J6	ACAM-J6	ACAM-J6	ACAM-J6	ACAM-J6
Acc	0.6437	0.6342	0.6778	0.7585	0.6318							0.8030
CK	0.2270	0.1461	0.1470	0.4613	0.1704							0.5158
AUC	0.6918	0.6770	0.7194	0.8049	0.6596							0.8433
Precision	0.6524	0.6391	0.6967	0.7838	0.6482							0.8267
Recall / Sens.	0.6568	0.6457	0.7079	0.7996	0.6571							0.8394
F1	0.6546	0.6424	0.7022	0.7916	0.6526							0.8330
Specificity	0.6306	0.6227	0.6477	0.7174	0.6065							0.7666
p-Value	<0.001	<0.001	<0.001	0.021	<0.001							0.019

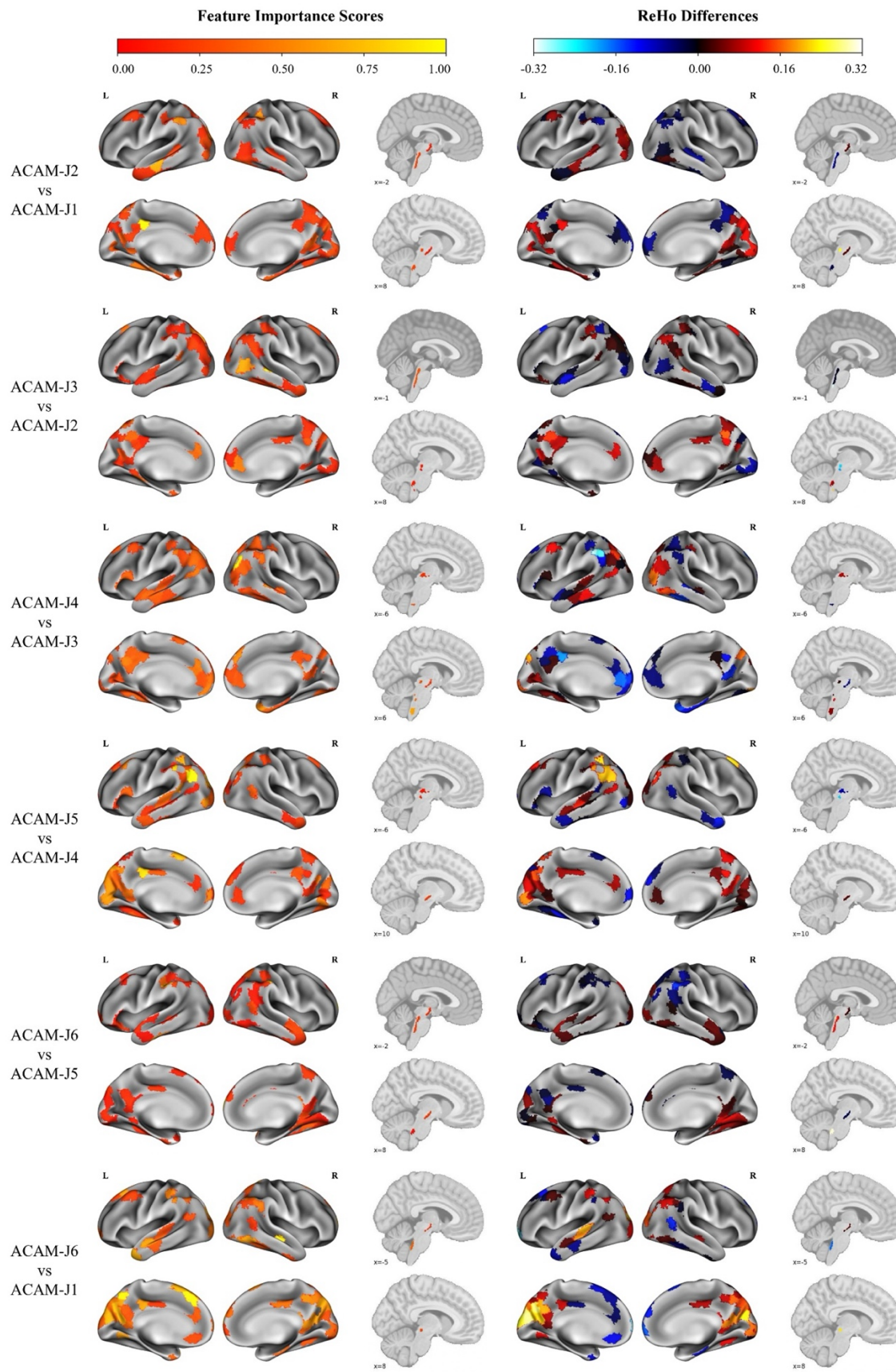


**Fig. 4: Brain-plots for pairwise ACAM-J transitions.** Left panels denote feature-significant analysis highlighting the cortical and subcortical ROIs identified via the pairwise feature significance analysis, with the color bar indicating normalized feature-importance scores. Right panels show axial and coronal slices of the average ReHo difference between each comparison, with the color bar indicating ReHo differences, with warm colors marking increased synchronization in ACAM-J. Only ROIs selected by permutation-based significance across all folds are displayed, emphasizing consistent discriminators within default-mode, control, salience networks, and the locus coeruleus (see Table 2 for evaluation metrics).

## ROI overlap maps

To further delineate critical brain regions necessary for differentiating ACAM-J from non-meditative control conditions and cognitive tasks, lesion overlap analysis was conducted. **Fig. 5** presents these overlap maps, identifying regions whose disruption significantly impacted classification accuracy, confirming the essential roles of the prefrontal cortex, anterior cingulate cortex, insula, and parietal lobes—areas integral to attention, emotional processing, interoceptive awareness, and spatial cognition, respectively. The appearance of Prefrontal Cortex — Involved in attention and executive function<sup>25</sup>, Anterior Cingulate Cortex — Associated with self-regulation and emotional processing<sup>26</sup>, Insula — Linked to interoceptive awareness and salience tagging<sup>27</sup>, Parietal Lobes — Related to spatial awareness and attentional orienting, and Locus Coeruleus — Critical for noradrenergic arousal modulation<sup>16</sup> show that these hubs jointly underpin the discriminative neural patterns observed across ACAM-J.

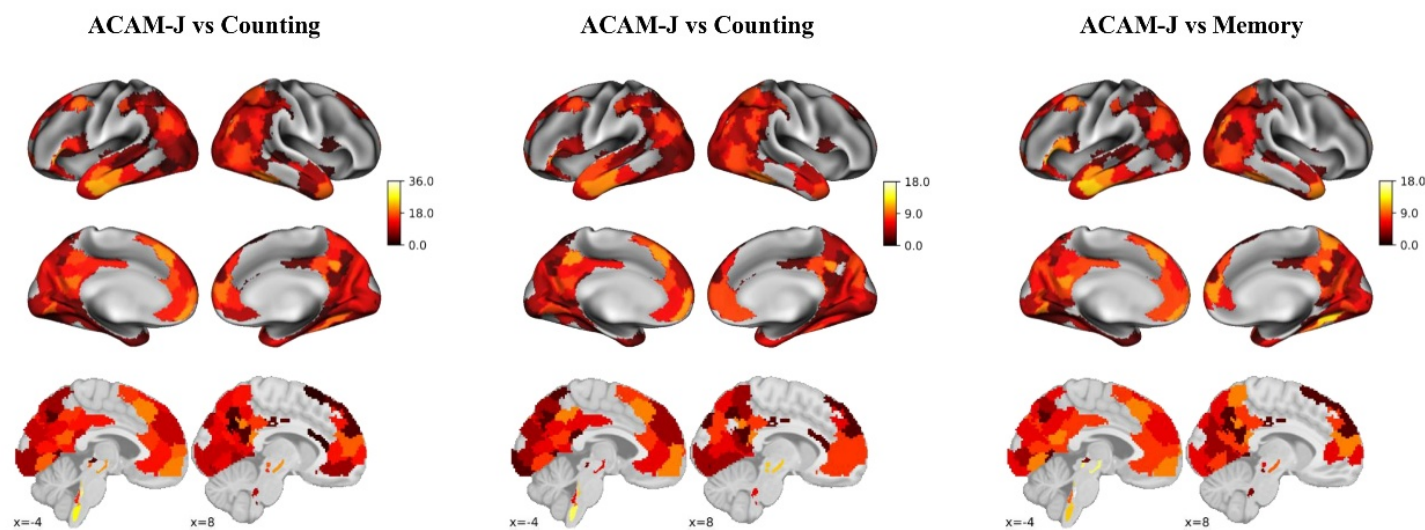


**Fig. 5: ROI Overlap Maps with cortical (above) and subcortical (below) plots. Bar plots indicate, for each ROI, the number of classifiers whose accuracy dropped when that region's ReHo feature was removed in leave-one-region-out analyses across ACAM-J vs. control, counting, and memory comparisons. Brighter colors (prefrontal, cingulate, insula, parietal) identify regions most critical to classification performance.**

## Residual Analysis

Classification on the revised data improved accuracy from 65.87% to 66.82%. These findings reinforce the need to control and account for individual variation in phenomenology during classification<sup>5,17</sup>. The changes in accuracy and Cohen's Kappa scores before and after residual analysis are shown in **Fig. 6**.

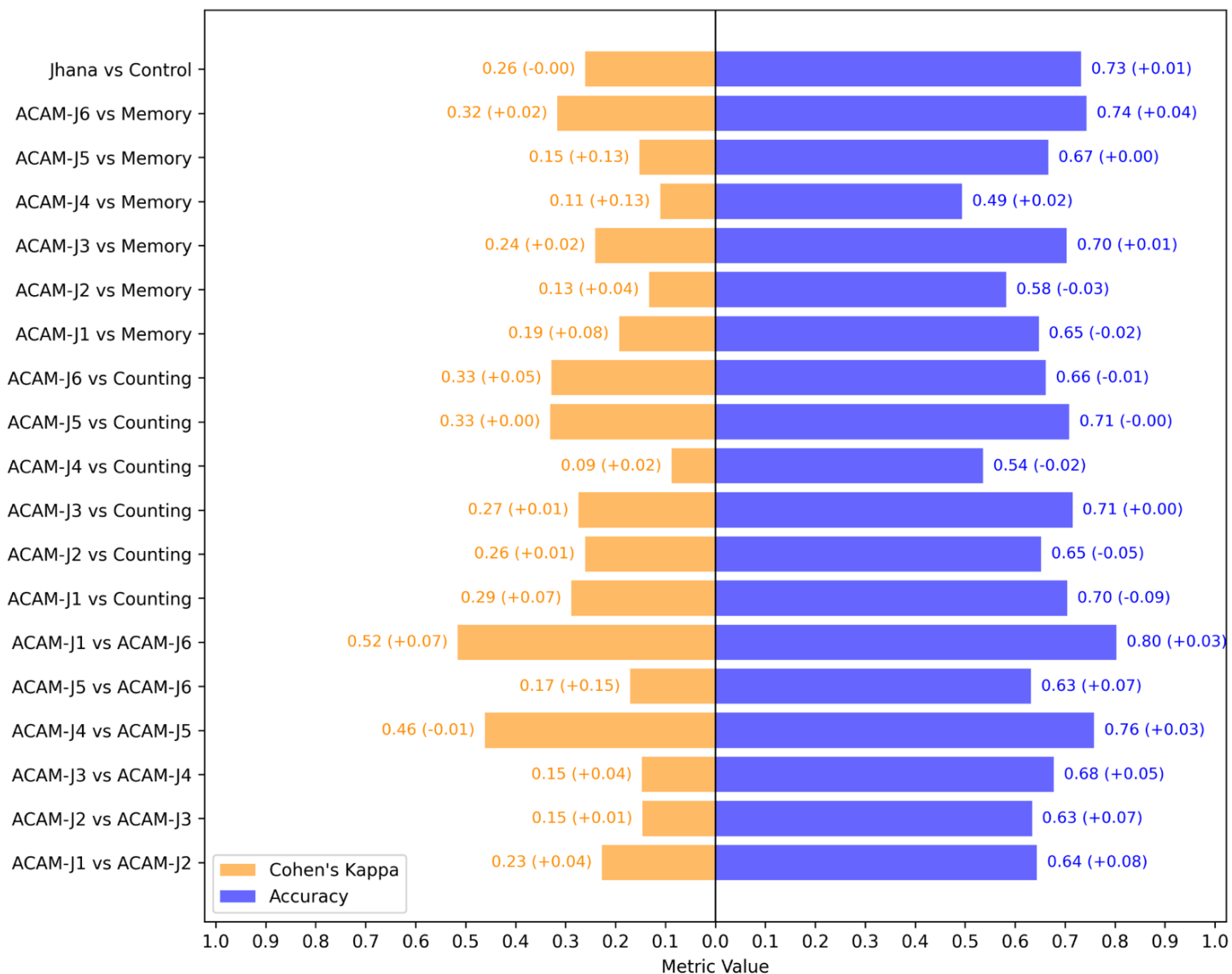


**Fig. 6: Summary of Accuracy and Cohen's Kappa Scores.** Clustered bars display overall accuracy and Cohen's  $\kappa$  for each binary comparison, with bracketed annotations indicating the gain in Cohen's Kappa and Accuracy resulting from removing phenomenological variance via residual analysis.

### Summary of the results

Collectively, the machine learning classification analysis across all comparisons has yielded an overall average accuracy of 66.82% and an overall average Cohen's Kappa of 0.2443, with all comparisons reaching statistical significance ( $p < 0.05$ ). The integrated findings summarized visually in **Fig. 6** highlight the capability of ReHo-derived neural patterns to reliably discriminate between ACAM-J and non-meditative conditions, supporting the utility of machine learning approaches in elucidating the neural underpinnings of advanced concentrative absorption meditation.

### 3. Discussion

In this study, we developed a machine learning pipeline, explicitly informed by first-person phenomenological reports, that successfully distinguish the progressive states of ACAM-J using fMRI data. To our knowledge, this is not only the first

demonstration of predictive models capable of decoding ACAM-J in MRI. Beyond establishing the feasibility of ACAM-J decoding, this work offers a powerful methodological framework for studying rare or difficult-to-detect cognitive states beyond advanced meditation. Our findings pave the way for translational applications, including developing tangible neural biomarkers to guide clinical interventions such as neurofeedback, and individualized monitoring of meditative or therapeutic training. More broadly, this approach outlines a scalable roadmap for efforts aimed at mapping human consciousness.

### Tailored machine learning pipeline for rare cognitive states

Rather than treating rarity as a methodological obstacle, our approach treats it as a defining property of the cognitive phenomena under investigation. ACAM-J is not only uncommon in the general population, but are also characterized by subtle, internally stabilized experiential dynamics that unfold over training and practice. Capturing such states therefore requires analytical frameworks optimized for precision, interpretability, and robustness under constrained sampling conditions<sup>28,29</sup>.

To this end, we designed a machine-learning pipeline that integrates established practices and necessary methodological adaptation to ensure robust classification<sup>28,29</sup>, including Synthetic Minority Oversampling Technique (SMOTE), stratified cross-validation, RFE, and an ensemble-based approach. SMOTE was employed as a principled means of stabilizing decision boundaries in underrepresented absorption states, allowing classifiers to better approximate the latent structure of the data<sup>28,29</sup>. Stratification maintained the class distributions of ACAM-J across folds, preserving the structure of the dataset. Interpretability was treated as a core design constraint rather than a post hoc add-on. RFE enabled identification of crucial brain regions contributing most strongly to classification performance without imposing strict assumptions about feature dominance or hierarchical ordering. This strategy aimed to bolster interpretability while preserving model flexibility.

Model stability and generalization were further reinforced through early stopping procedures and ensemble learning. Early stopping monitored performance metrics on a validation split, halting training when subsequent iterations failed to yield improvements. This procedure effectively kept our models from overfitting the training data while maintaining generalization to unseen samples. Ensemble methods reduced sensitivity to idiosyncrasies of individual models and enhanced robustness across repeated experiments by aggregating predictions across multiple classifiers. The consistent emergence of *k*-Nearest Neighbors, Logistic Regression, and Neural Networks reflects the adaptability of these models to complex, high-dimensional nature of neuroimaging data. Taken together, this pipeline demonstrates how carefully constrained machine-learning strategies can reveal reliable neural distinctions even in small samples and rare cognitive states such as ACAM-J.

### A neural model of advanced concentrative absorption

Our findings support a network-level model for profound states of concentrative absorption characterized by a dynamic interaction between large-scale brain networks<sup>6,20</sup>. The discriminative features identified across ACAM-J, including the brainstem locus coeruleus (LC), salience, control (e.g., prefrontal cortex and cingulate), and default mode (e.g., medial prefrontal, precuneus, and posterior cingulate cortex) networks.

A central insight of our model is the recalibration of arousal–attention coupling. Increased LC contribution at later ACAM-J aligns with its established role in arousal regulation and with ultra-high-field MRI evidence characterizing structural connectivity of brainstem autonomic nuclei in living humans<sup>30</sup>. Hence, LC activity likely reflects a refined autonomic state of stable wakefulness with minimal arousal, consistent with accounts of “effortless alertness” in advanced concentrative absorption<sup>31</sup>. In parallel, the salience network becomes increasingly prominent, suggesting that practitioners increasingly rely on this system to maintain precise contact with the meditative object while minimizing intrusion of mental proliferation<sup>25,27</sup>. The contribution of salience-related regions is not indicative of effortful control, but rather of a finely tuned detection-and-stabilization process. This interpretation aligns with neurophenomenological evidence that deep absorption depends not on effortful suppression, but on the stable maintenance of an attentional attractor state<sup>9,31</sup>.

In contrast, regions of the anterior DMN become less central in distinguishing deeper ACAM-J. This attenuation is consistent with reduced self-referential processing, decreased language-related coupling, and diminished spontaneous mentation documented in long-term practitioners<sup>32,33</sup>. Notably, this reduction is already evident by ACAM-J4, which phenomenologically marks the culmination of form-based absorption<sup>10</sup>. At this stage, self-referential activity appears to be largely minimized, suggesting that the decoupling of narrative self-processing precedes the transition to formless absorption rather than emerging only at later, more abstract ACAM-J. Control networks, including dorsolateral prefrontal and cingulate cortices, remain integral for sustaining attention<sup>34</sup>, an important characteristic of ACAM-J. Together, these network shifts support a model in which concentrative absorption emerges from heightened alertness, strengthened object-based salience, sustained attentional stability, and reduced self-generated cognition.

More importantly, incorporating self-reported phenomenological data into our classification pipeline further isolated neural changes specifically attributed to ACAM-J<sup>26</sup>. Regressing out variance associated with phenomenology, residual-based analysis effectively boosted overall classification accuracy by 0.95%, highlighting how unmodeled phenomenological influences had previously obscured ACAM-J-specific neural signatures. This integrative approach carries significant implications for the field, providing concrete evidence that combining objective neural measures with structured subjective reports to achieve a more nuanced understanding of complex cognitive states such as ACAM-J<sup>4,5,26</sup>.

## Potential applications

The data-driven framework introduced here offers multiple translational avenues for leveraging ACAM-J biomarkers to design interventions, technologies, and experimental paradigms capable of cultivating or monitoring advanced meditative absorption. Neural markers identified for ACAM-J may inform targeted non-invasive neuromodulation paradigms such as neurofeedback protocols<sup>16</sup>. For example, real-time feedback of activity in posterior and prefrontal regions could help individuals facing attentional lapses to progressively attain advanced concentration. Such approaches may support practitioners in stabilizing concentration and detecting incipient attentional lapses before subjective awareness alone would permit correction. Non-invasive neuromodulation (e.g., TMS, tDCS) could be deployed to modulate arousal, salience, or control systems identified by

the model, enabling mechanistic tests of how these networks contribute to sustained absorption<sup>16</sup>. When combined with real-time classification, such interventions naturally lend themselves to closed-loop designs that synchronize neural data with first-person reports, allowing moment-to-moment tracking of state transitions<sup>4,17,35,36</sup>. More broadly, embedding ACAM-J-derived markers as objective endpoints in clinical and contemplative trials could help quantify dose–response relationships and individual trajectories<sup>4</sup>. Embedding these markers into longitudinal designs could allow quantification of dose–response relationships, individual learning trajectories, and inter-individual variability in absorption capacity.

## Challenges and Future Directions

A key limitation of this study is the relatively small number of participants capable of entering and maintaining ACAM-J. Later ACAM-J, in particular, are rare and challenging to sustain, resulting in fewer usable data samples. This constraint inevitably limits the generalizability of our findings and the ability to capture individual variability in meditation depth and neural patterns. Although data-balancing strategies such as SMOTE helped mitigate class imbalance<sup>28,37</sup>, synthetic augmentation cannot fully recapitulate the nuanced, heterogeneous neural signatures associated with advanced meditative absorption. As a result, models trained on SMOTE-enhanced datasets remain at risk of overfitting and may not always generalize to new participants or sessions.

These constraints also informed our decision to prioritize classical, interpretable machine learning methods over deep learning approaches, which typically require substantially larger datasets and risk collapsing under small-N conditions<sup>38</sup>. While this choice improves reproducibility and transparency, it also caps the upper bound of model complexity and limits our ability to test architectures that may better capture nonlinear or distributed patterns. As larger datasets become available, future work may explore hybrid pipelines, transfer learning, and representation learning that leverage pre-trained models or multimodal embedding spaces to detect subtle cognitive states. Implementing standardized micro-phenomenological reporting could strengthen correlations with objective brain signatures<sup>17,39</sup>. Expanding into multimodal designs integrating fMRI with EEG, MEG, or diffusion imaging will be critical for resolving both spatial and temporal dynamics of ACAM-J<sup>6,20,22</sup>.

## Conclusion

This study demonstrates that advanced concentrative absorption states can be systematically decoded from fMRI data using machine-learning approaches grounded in first-person phenomenology. We developed a pipeline tailored to rare, expertise-dependent cognitive states, integrated structured phenomenological reports, and decoded subtle advanced meditation states. The findings contribute to the understanding of the neural mechanisms underlying advanced meditation and highlight the potential of machine learning in contemplative neuroscience. Our approach demonstrates feasibility in predictive modeling of advanced meditation and offers a roadmap for future multimodal and large-scale studies. More broadly, these results highlight how

carefully designed machine learning can expand the empirical research of contemplative neuroscience, opening new avenues for mechanistic, translational, and theoretical inquiry into the upper bounds of human consciousness.

#### 4. Methods

**Fig. 7** presents an overview of the ACAM-J ML classification pipeline, which consists of five sequential modules. Module I covers data collection and preprocessing, including data acquisition, standard preprocessing steps, and ReHo calculation. Module II focuses on feature engineering and selection by applying SMOTE to balance the dataset and identifying relevant features based on prior studies<sup>9</sup> and Recursive Feature Elimination (RFE). Module III implements the machine learning procedures, integrating multiple algorithms with five-fold stratified cross-validation and ensemble learning. Module IV evaluates model performance using case-study data, and Module V analyzes feature significance by generating brain maps that highlight the most critical regions for ACAM-J classification. The following sections describe each module in detail.

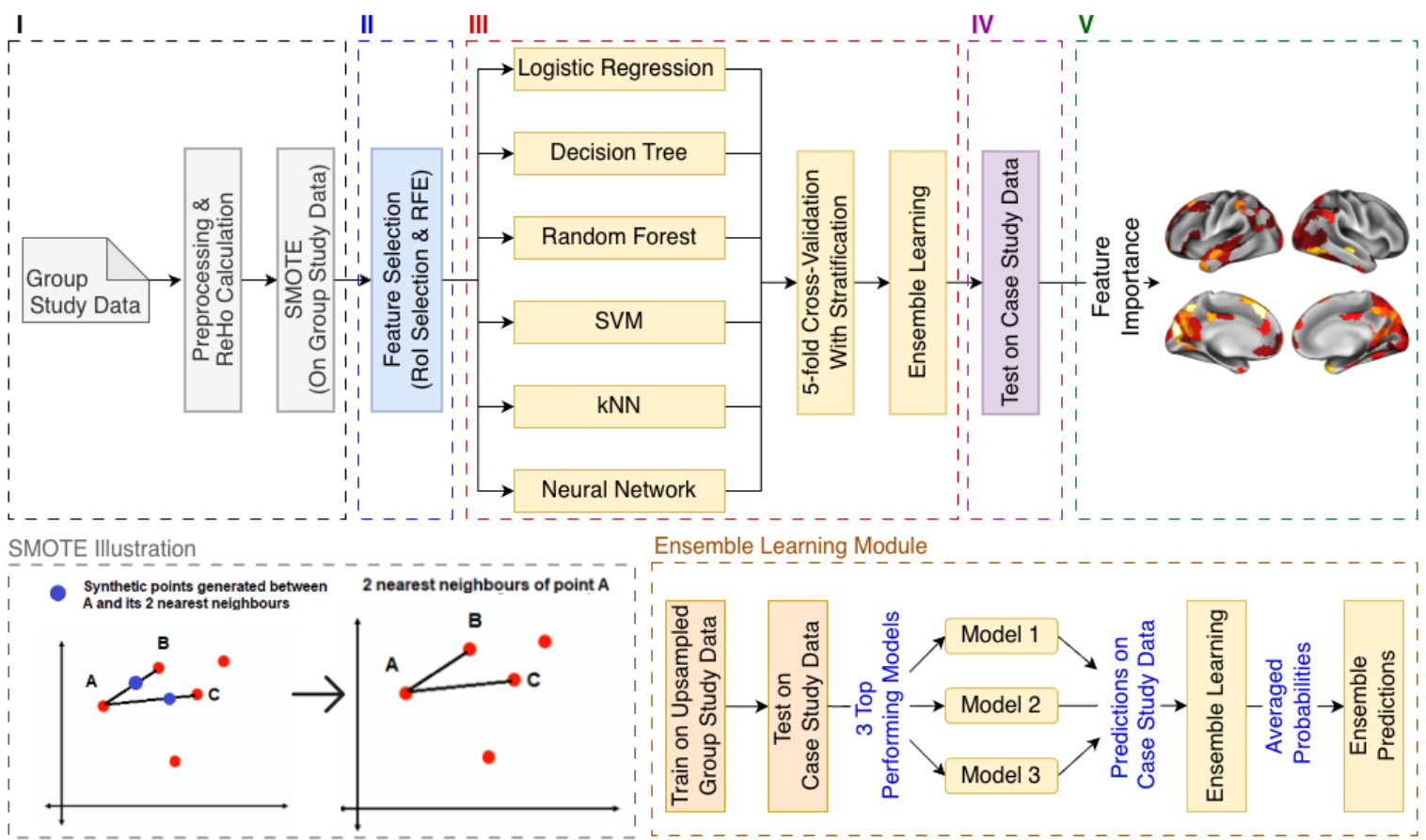


**Fig. 7: Machine Learning Pipeline for Classifying ACAM-J, consisting of five modules** I. Data Collection and Preprocessing; II: Feature Engineering and Selection; III: Machine Learning; IV: Model Testing and Evaluation; V: Feature Significance Analysis. Ensemble Learning and SMOTE modules are elaborated separately. It illustrates raw fMRI acquisition and ReHo computation; ROI balancing via SMOTE and pruning via RFE; ensemble classifier training under 5-fold stratified cross-validation; a two-step group- and case-study evaluation scheme; and

*derivation and aggregation of normalized feature-importance metrics across models. Implementation specifics are elaborated in the Supplementary Section.*

## Participants and preprocessing

### Participants

The study combined data from two complementary cohorts, a case study participant from our previous work<sup>9</sup>, and group-level cohort data. The case study participant was a white American male adept meditator who was 52 years old at the time of the study. The participant was a long-term meditation teacher with over 25 years of meditation experience. Based on an estimated one to two hours of daily practice since the start of practice, and approximately a cumulative one year of retreat at 14 hours per day, we estimate a total practice amount of at least 20,000 hours.

20 participants (19 males, 1 female) from well-established meditation communities, all of whom demonstrated advanced expertise in ACAM-J meditation practices, were recruited for the group-cohort study. On average, the age range in this sample was 26-67 years old (mean age =  $43.95 \pm 15.10$  years). On average, participants had  $17.40 \pm 11.59$  years of meditation experience and reported an estimated total of  $20500.40 \pm 17288.98$  hours of dedicated meditation practice. The study received approval from the Mass General Brigham Institutional Review Board (IRB), and the participant provided informed consent.

## Experimental design

Both case study and group-level data were collected following the protocol outlined in our previous study<sup>9</sup>. Below is a summary of the data collected from the cohort study.

### ***Advanced concentrative absorption meditation (ACAM-J)***

Participants followed their standard ACAM-J sequence with closed eyes, progressing from access concentration through ACAM-J1 to ACAM-J8, concluding with a post-ACAM-J8 state referred to as afterglow. We requested participants to stay within any ACAM-J for at least 3 minutes for reliable computation of fMRI metrics<sup>40</sup>. For participants with ACAM-J duration of less than 3 minutes, we conducted another session of ACAM-J. The participants marked transitions from access concentration to ACAM-J8 with a button press. Note that 2 participants, including one from the case study, did not indicate transitions from ACAM-J6 to ACAM-J7 nor from ACAM-J7 to ACAM-J8, as it would disrupt the natural flow of ACAM-J practice for them. Please see<sup>31</sup> for additional details.

### ***Non-meditative control tasks***

Two non-meditative control conditions were developed for comparison with meditation states, aimed at engaging the participant's mind in non-meditative, everyday cognitions while avoiding the induction of meditative states. Resting-state control task was not used due to concerns that experienced meditators might enter meditative states during rest, which may complicate interpretations of results<sup>41</sup>. These control conditions consider the phenomenology of meditative states and the nature of the experimental paradigm to ensure greater consistency and reliability in the data<sup>9</sup>. The two control conditions involved a memory task, where the participant recalled events from the past one week, and a counting task, where the participant mentally counted down from 10,000 in decrements of 5. For most participants, one 8-minute run of each control task was collected. A subset of participants completed a second set of control runs because they were also involved in a separate case study that required two sets of control conditions.

### ***Phenomenology***

To complement objective neuroimaging data, this study design also used a first-person phenomenological approach, in which the subject assessed the mental and physiological processes relevant to the experience of ACAM-J as they manifested during meditation. In brief, following a complete ACAM-J run (ACAM-J1 to ACAM-J8), the participant assigned a rating from 1 to 10 for phenomenological items including: (1) stability of attention, ranging from poor to excellent stability; (2) width of attention, varying from a narrow scope like a laser to very wide like a fisheye lens; (3) intensity of ACAM-J, indicating how intense a specific ACAM-J quality was; (4) early phenomenology of sights, sounds, physical sensations, and narrative thought stream, denoted by the presence of sights, sounds, physical sensations, and narrative thought contents during the form ACAM-J (ACAM-J1-J4); and (5) late phenomenology of sights, sounds, physical sensations, and narrative thought stream, characterized by the presence of sights, sounds, physical sensations, and narrative thought contents during the formless ACAM-J (ACAM-J5- J8). Higher rating values indicated a more robust experience within the given item. Stability of attention, width of attention, and intensity of ACAM-J were rated for each ACAM-J. Phenomenology of sights, sounds, physical sensations, and narrative thought stream were rated separately for early (ACAM-J1-J4) and late (ACAM-J5-8) aggregate states.

### ***Neuroimaging acquisition and preprocessing***

Following the detailed protocols in<sup>9</sup>, neuroimaging scans were obtained utilizing a 7T magnetic resonance (MR) scanner (SIEMENS MAGNETOM Terra) equipped with a 32-channel head coil. Functional imaging utilized a single-shot two-dimensional echo planar imaging sequence with T2\*-weighted BOLD-sensitive MRI. Whole-brain T1-weighted structural images were also acquired with the same parameters as the case study<sup>9</sup>. Physiological signals,

including heart rate (measured using pulse oximetry) and respiration (recorded with breathing bellows), were continuously monitored throughout the scanning session.

Preprocessing of fMRI followed standard preprocessing steps and encompassed the following: (1) de-spiking, (2) RETROspective Image CORrection (RETROICOR), (3) slice time correction, (4) distortion correction, (5) motion correction, (6) registration of the anatomical dataset (T1w) to a standard MNI template, (7) scrubbing and removal of any volume with motion  $>0.3$  mm and more than 5% outlier voxels, (8) regression of eroded cerebrospinal fluid (CSF) mask time course and motion parameters (3 translations, 3 rotations) per run, and finally band-pass filtering (0.01–0.1 Hz). Each fMRI run was then partitioned into distinct segments corresponding to different ACAM-J.

### Regional homogeneity (ReHo) calculation

ReHo is a measure of similarity in temporal activation pattern of a voxel and its nearby voxels<sup>9,42,43</sup>. This measure of local functional connectivity within brain regions is a close derivative of underlying brain activity. A higher ReHo value indicates stronger synchronization of local brain regions, indicating greater functional connectivity in that region and thus an index of greater brain activity. In this study, we defined a cluster size of 27 and calculated the ReHo values for each fMRI segment, standardized the ReHo values before smoothing the standardized ReHo maps using a 2 mm full-width half-maximum (FWHM) kernel. The standardized ReHo values were then parcellated using the four different parcellation/segmentation schemes<sup>44–47</sup>, yielding 498 ReHo values for each fMRI segment as described in Table 1. We used 400 cortical ROIs from the Schaefer atlas, 32 subcortical ROIs from the Tian atlas, 54 brainstem ROIs from the Bianciardi atlas, and 10 cerebellar ROIs from the MDTB atlas, for a total of 498 ROIs.

### SMOTE for data imbalance handling

Our dataset exhibits a marked imbalance: the case study participant contributed 194 samples (27 ACAM-J runs and 16 runs each for counting and memory), whereas the cohort study contributed only 161 entries. This leads to an approximate 27:1.4 ratio between the case and cohort data, which can bias model training and compromise generalizability. To address this, we employed both data-level and algorithm-level solutions.

#### *Data-level balancing with SMOTE*

We first applied the Synthetic Minority Over-sampling Technique (SMOTE), illustrated in **Fig. 7**, to the group study dataset<sup>28,37,48</sup>. SMOTE generates new minority-class samples by interpolating existing instances, thus reducing class imbalance without simply replicating data points.

Before applying SMOTE, certain ACAM-J and control tasks were severely underrepresented relative to the case study participant. For example, individual classes in the cohort often contained only a handful of samples compared to the much larger number contributed by the case study participant, contributing to the overall 27:1.4 imbalance. After applying SMOTE, classes were balanced at a 1:1 ratio, allowing the model to learn a richer decision boundary and mitigating overfitting to the majority class.

We first trained and selected models using only the group-study dataset, after balancing it with SMOTE. Specifically, (1) we split the group-study data into training/validation folds, (2) within each fold we applied SMOTE only to the training portion to equalize class representation, and (3) we trained candidate classifiers on this SMOTE-balanced training data and evaluated them on the unmodified validation data. This fold-wise procedure yields decision boundaries that are not dominated by majority classes while avoiding data leakage into validation.

After cross-validation and model selection, we formed the final ensemble by combining the top-performing models (selected by validation performance) and refitting this ensemble on the full SMOTE-balanced group-study dataset. We then performed a single held-out evaluation by testing the final ensemble on the original, unmodified case-study dataset. This two-step strategy (training on balanced group data, testing on original case data) ensures that reported performance reflects generalization to the real distribution rather than artifacts of resampling.

In practice, augmentation in the group-study training data was not limited to SMOTE alone. After SMOTE generated synthetic samples by interpolating between nearest neighbors in feature space, we further introduced controlled variability to avoid exact duplication and to better reflect plausible feature fluctuations. Concretely, we applied (i) light stochastic perturbations to numeric features using a `noise_level` parameter, (ii) blending of original and perturbed values controlled by `'retention_degree'`, and (iii) additional interpolation applied to a subset of numeric columns controlled by `'interpolation_proportion'`. Together, these steps produce augmented samples with realistic variability, while the case-study test set remains completely unmodified.

## Feature selection

We first selected a subset of ROIs from the 498 parcellated ROIs based on three key criteria: (1) prior results from demonstrating significant trends across ACAM-J and clear differentiation from non-meditative control conditions<sup>9</sup>; (2) regions exhibiting reliable and stable ReHo values as determined through network intra-class correlation analyses<sup>5</sup>; and (3) ROIs with established functional relevance to ACAM-J, particularly those involved in attentional regulation, sensory processing, self-referential cognition, and reward circuitry<sup>10</sup>. This approach ensured our analysis focused on regions with both empirical and theoretical significance to ACAM-J.

We then applied Recursive Feature Elimination (RFE) with a Random Forest model to identify the most informative neural features distinguishing ACAM-J from control tasks<sup>49</sup>. RFE was chosen over other feature selection methods, such as filter-based methods or embedded approaches, for its interpretability, ability to consider feature interactions, and effectiveness with noisy and complex data<sup>50,51</sup>. RandomForest was preferred due to its robustness, resistance to overfitting, and ability to handle nonlinear relationships in small and variable datasets<sup>50,52,53</sup>. Features with normalized importance scores below 0.5 were removed iteratively until only the most relevant features remained.

### ***Machine learning module***

We applied several ML models to classify ACAM-J, chosen for their interpretability and suitability to neuroimaging data.

#### **Logistic regression**

Logistic Regression models the probability of categorical outcomes through a logistic function, making it ideal for classification tasks<sup>54</sup>. Its coefficients are interpretable, directly indicating the strength and direction of the relationship between each feature and the predicted outcome, thus providing transparency for clinical and neuroscientific interpretations.

#### **Decision trees**

Decision trees partition the feature space into discrete segments through hierarchical decision rules, offering intuitive visualization of the decision-making process<sup>55</sup>. Their simplicity and interpretability are particularly valuable in exploratory neuroscience studies, identifying critical brain regions influencing meditation states.

#### **Random forest**

Random forest, an ensemble of decision trees, enhances prediction accuracy by averaging outcomes from multiple decision trees trained on bootstrapped datasets<sup>50</sup>. It uses robust feature importance metrics, mean decrease in impurity and accuracy, which could be helpful for identifying significant neurobiological correlates of meditation states.

#### **Support vector machines (SVM) with linear kernels**

SVMs with linear kernels efficiently separate classes using a hyperplane optimized for high-dimensional datasets, common in neuroimaging<sup>56</sup>. This method requires minimal hyperparameter tuning and offers straightforward interpretation of results, making it well-suited for our neuroimaging analysis.

### k-nearest neighbors (kNN)

kNN classifies samples based on the majority class among nearest neighbors in feature space<sup>57</sup>. Without a training phase, kNN adapts flexibly to varying data structures, accommodating the diversity and variability inherent in neuroimaging data.

### Artificial neural networks (ANN)

ANN, specifically multi-layer perceptrons, model complex, nonlinear relationships between input and output layers<sup>58</sup>. Despite being computationally intensive, their ability to capture intricate neural patterns is highly beneficial for exploring nuanced meditation-induced brain activity.

We have excluded Gradient Boosting Machines (GBM) and related ensemble methods like XGBoost, AdaBoost, and LightGBM<sup>59,60</sup> because we are already using an ensemble strategy. Moreover, Naive Bayes and non-linear SVM kernels have not been used due to their unsuitability for our dataset's characteristics and our focus on maintaining methodological simplicity<sup>61</sup>. Deep learning methods have also been omitted to avoid overfitting, given the small size and high complexity of our data<sup>38</sup>. Techniques like clustering and dimensionality reduction were not aligned with our study objectives, and reinforcement learning was considered irrelevant to our goals<sup>62</sup>.

### Model training with stratified cross-validation

We used stratified cross-validation, which preserves class proportions in every fold, to train the SMOTE-balanced dataset<sup>63</sup>. Stratification ensures that both original and synthetic samples remain evenly distributed across folds, preventing any fold from being dominated by a particular class<sup>37,64</sup>. Importantly, stratification fosters more robust model estimates, as each fold remains representative of the entire dataset, thereby enhancing overall performance metrics<sup>65</sup>. Beyond balancing class distributions, stratification maintains consistent subject representation, avoiding subject-specific overfitting and ensuring that models learn generalizable patterns rather than idiosyncrasies tied to individual meditators or biases introduced by data augmentation<sup>64</sup>. While early stopping mechanisms have also been implemented to counteract overfitting, they prove unnecessary, as validation performance remains stable after peaking. Thus, preserving stratification post-upsampling has further strengthened the reliability of our models in handling imbalanced data<sup>28,65</sup>.

### Handling overfitting

To mitigate and assess overfitting risks, we introduced diversity through SMOTE and leveraged stratification to keep class ratios consistent across folds. We also used a broad set of evaluation metrics, including requiring *p*-values

below 0.05 and Cohen's kappa above 0.0-to provide statistical evidence of model reliability and generalizability.

Emphasis was placed on test-set performance to ensure the models' applicability to unseen data. Lastly, we prepared Early Stopping<sup>66</sup> to halt training should validation performance degrade after a peak; however, no such decline occurred, rendering this step unnecessary.

## Ensemble learning

To further improve predictive performance and reduce variance through the aggregation of multiple learners, we implemented ensemble learning by combining the predictions of multiple ML models<sup>67,68</sup>. After training all candidate classifiers, we selected the top three models based on their accuracy and averaged their predicted probabilities to generate final ensemble outputs. Probability averaging was chosen for its simplicity, transparency, and stability<sup>68</sup>. While other ensemble strategies like weighted averaging or majority voting could be used, probability averaging provides a balanced and interpretable solution by integrating model confidence into the final prediction, enhancing overall performance requiring additional hyperparameters or weighting schemes. Ensemble outputs were then evaluated with the metrics.

## Model testing and evaluation

### *Testing strategy and parameter setting*

To ensure robust evaluation of our models, we employed a systematic testing strategy that follows a two-step validation process. All models were first trained and validated exclusively on the SMOTE-balanced group dataset using 5-fold stratified cross-validation to maintain proportional class representation across folds and ensure stable estimates of out-of-sample performance. After model selection, the final ensemble was tested on the unmodified case-study dataset. This allowed us to assess predictive performance on the natural distribution of ACAM-J states and control conditions, providing a stringent test of generalizability. Hyperparameters for each model type were optimized using grid search within the cross-validation framework. Following optimization, ensemble learning was applied by averaging predicted probabilities from the three best-performing models.

### *Evaluation metrics*

We assessed model performance using a complementary set of classification metrics to capture different aspects of predictive accuracy and reliability. Overall effectiveness was quantified using accuracy, while Cohen's kappa provided a chance-adjusted measure of agreement between predicted and true labels<sup>69</sup>. Discriminative ability across

decision thresholds was assessed using the area under the ROC curve (AUC). Precision and recall (sensitivity) captured the model's reliability in identifying positive instances, and the F1 score summarized their balance under class imbalance. Specificity was included to evaluate the correct identification of negative cases, thereby accounting for false-positive risk. Finally, *p*-values were calculated to assess the statistical significance of model performance, with values below 0.05 indicating that results were unlikely to arise from chance.

#### ***Pairwise feature significance analysis of ACAM-J and control tasks***

To characterize how neural features evolve with ACAM-J depth, we analyzed transitions between successive ACAM-J (e.g., ACAM-J1→J2, ACAM-J2→J3), as well as comparisons between ACAM-J and the non-meditative control tasks. These analyses capture both the gradual progression of concentrative absorption and the contrast between ACAM-J and baseline cognitive processes. We also examined a targeted comparison between ACAM-J1 and ACAM-J6 to capture the difference between early and late ACAM-J. This extreme contrast provides a stringent test of the model's capacity to discriminate early, content-rich states from advanced, highly abstract states, while also illustrating the nonlinear nature of meditative progression.

Feature significance was assessed using model-appropriate methods. For tree-based models (e.g., random forests, gradient boosted trees, decision trees), we used impurity-based feature importance to quantify each variable's contribution to split quality<sup>50,70</sup>. For linear models such as logistic regression and linear-kernel SVMs, feature coefficients were extracted to indicate the direction and magnitude of each ROI's influence on classification<sup>70</sup>. For models without built-in feature impact metrics, such as *k*-Nearest Neighbors, Neural Networks, or SVC with non-linear kernels, we applied “permutation importance”. This model-agnostic method evaluates a feature's importance by noting the change in model performance when the values of that feature are randomly shuffled<sup>71,72</sup>. All importance values were normalized to a 0-1 range to standardize interpretability across model types and to enable direct comparison of the most discriminative features.

#### ***Additional control analysis***

Given that phenomenological experiences were associated with brain activity during ACAM-J<sup>5,17</sup>, we performed additional analyses to account for individual differences in phenomenology. We used linear regression to regress out the effects of phenomenological measures from ReHo values. For each ROI, ReHo was treated as the dependent variable, and phenomenological variables were entered as predictors. Predictor variables included stability of attention and width of attention for both the ACAM-J and control tasks, as well as the quality of ACAM-J for the

ACAM-J task. The resulting residual ReHo values were then used as input to the same machine learning pipeline described above to examine how controlling phenomenology affected classification performance

## Data availability

The data supporting this study is available from the corresponding author upon reasonable request, subject to Institutional Review Board approval and in accordance with the data-sharing policies of the IRB-granting institution (Massachusetts General Hospital).

## Code Availability

The code for this study is available at <https://github.com/MIntelligence-Group>

## References

1. Sacchet, M. D., Fava, M. & Garland, E. L. Modulating self-referential processing through meditation and psychedelics: is scientific investigation of self-transcendence clinically relevant? *World Psychiatry* **23**, 298–299 (2024).
2. Kang, C. & Whittingham, K. Mindfulness: A Dialogue between Buddhism and Clinical Psychology. *Mindfulness* **1**, 161–173 (2010).
3. Tang, Y.-Y., Hölzel, B. K. & Posner, M. I. The neuroscience of mindfulness meditation. *Nat Rev Neurosci* **16**, 213–225 (2015).
4. Galante, J. *et al.* A Framework for the Empirical Investigation of Mindfulness Meditative Development. *Mindfulness* **14**, 1054–1067 (2023).
5. Ganesan, S., Yang, W. F. Z., Chowdhury, A., Zalesky, A. & Sacchet, M. D. Within-subject reliability of brain networks during advanced meditation: An intensively sampled 7 Tesla MRI case study. *Human Brain Mapping* **45**, e26666 (2024).
6. Potash, R. M. *et al.* Investigating the complex cortical dynamics of an advanced concentrative absorption meditation called jhanas (ACAM-J): a geometric eigenmode analysis. *Cerebral Cortex* **35**, bhaf039 (2025).
7. Sparby, T. & Sacchet, M. D. Toward a Unified Account of Advanced Concentrative Absorption Meditation: A Systematic Definition and Classification of Jhāna. *Mindfulness* **15**, 1375–1394 (2024).
8. Wright, M. J., Sanguinetti, J. L., Young, S. & Sacchet, M. D. Uniting Contemplative Theory and Scientific Investigation: Toward a Comprehensive Model of the Mind. *Mindfulness* **14**, 1088–1101 (2023).
9. Yang, W. F. Z. *et al.* Intensive whole-brain 7T MRI case study of volitional control of brain activity in deep absorptive meditation states. *Cerebral Cortex* **34**, bhad408 (2024).
10. Yang, W. F. Z., Sparby, T., Wright, M., Kim, E. & Sacchet, M. D. Volitional mental absorption in meditation: Toward a scientific understanding of advanced concentrative absorption meditation and the case of jhana. *Helyon* **10**, e31223 (2024).

11. Sparby, T. & Sacchet, M. D. The Third Wave of Meditation and Mindfulness Research and Implications for Challenging Experiences: Negative Effects, Transformative Psychological Growth, and Forms of Happiness. *Mindfulness* **16**, 2156–2170 (2025).
12. Sparby, T. & Sacchet, M. D. Toward a Unified Model of Advanced Meditation, Human Development, Meditation Maps, and Transtradition Metaphors: Facing Impermanence, Suffering, and Death. *Mindfulness* **16**, 2472–2482 (2025).
13. collins-steven. On the Very Idea of the Pali Canon. *The Open Buddhist University* [https://buddhistuniversity.net/content/articles/idea-of-the-pali-canon\\_collins-steven](https://buddhistuniversity.net/content/articles/idea-of-the-pali-canon_collins-steven) (2025).
14. Dhammadharo, A. L. Keeping the Breath in Mind & Lessons in Samādhi.
15. Mahāthera, H. G. The Jhānas In Theravada Buddhist Meditation.
16. Abellaneda-Pérez, K., Potash, R. M., Pascual-Leone, A. & Sacchet, M. D. Neuromodulation and meditation: A review and synthesis toward promoting well-being and understanding consciousness and brain. *Neuroscience & Biobehavioral Reviews* **166**, 105862 (2024).
17. Potash, R. M., Van Mil, S. D., Estarellas, M., Canales-Johnson, A. & Sacchet, M. D. Integrated phenomenology and brain connectivity demonstrate changes in nonlinear processing in jhana advanced meditation. Preprint at <https://doi.org/10.1101/2024.11.29.626048> (2024).
18. Chowdhury, A. *et al.* Multimodal neurophenomenology of advanced concentration absorption meditation: An intensively sampled case study of Jhana. *NeuroImage* **305**, 120973 (2025).
19. Demir, U., Yang, W. F. Z. & Sacchet, M. D. Advanced concentrative absorption meditation reorganizes functional connectivity gradients of the brain: 7T MRI and phenomenology case study of jhana meditation. *Cerebral Cortex* **35**, bhaf079 (2025).
20. Treves, I. N., Yang, W. F. Z., Sparby, T. & Sacchet, M. D. Dynamic brain states underlying advanced concentrative absorption meditation: A 7-T fMRI-intensive case study. *Network Neuroscience* **9**, 125–145 (2025).
21. Jordan, M. I. & Mitchell, T. M. Machine learning: Trends, perspectives, and prospects. *Science* **349**, 255–260 (2015).
22. Singh, S., Gupta, V., Reddy, T. K., Bhushan, B. & Behera, L. Meditation and Cognitive Enhancement: A Machine Learning Based Classification Using EEG. in *2022 IEEE International Conference on Systems, Man, and Cybernetics (SMC)* 1973–1978 (IEEE, Prague, Czech Republic, 2022). doi:10.1109/SMC53654.2022.9945131.
23. Hsu, A.-L. *et al.* Classification of mindfulness experiences from gamma-band effective connectivity: Application of machine-learning algorithms on resting, breathing, and body scan. *Computer Methods and Programs in Biomedicine* **257**, 108446 (2024).
24. Webb, C. A., Hirshberg, M. J., Davidson, R. J. & Goldberg, S. B. Personalized Prediction of Response to Smartphone-Delivered Meditation Training: Randomized Controlled Trial. *J Med Internet Res* **24**, e41566 (2022).
25. Kerr, C. E., Sacchet, M. D., Lazar, S. W., Moore, C. I. & Jones, S. R. Mindfulness starts with the body: somatosensory attention and top-down modulation of cortical alpha rhythms in mindfulness meditation. *Front. Hum. Neurosci.* **7**, (2013).
26. Sparby, T. & Sacchet, M. D. Defining Meditation: Foundations for an Activity-Based Phenomenological Classification System. *Front. Psychol.* **12**, 795077 (2022).
27. Giommi, F. *et al.* The (In)flexible self: Psychopathology, mindfulness, and neuroscience. *International Journal of Clinical and Health Psychology* **23**, 100381 (2023).
28. Haibo He & Garcia, E. A. Learning from Imbalanced Data. *IEEE Trans. Knowl. Data Eng.* **21**, 1263–1284 (2009).

29. T R, M. *et al.* The stratified K-folds cross-validation and class-balancing methods with high-performance ensemble classifiers for breast cancer classification. *Healthcare Analytics* **4**, 100247 (2023).

30. Singh, K. *et al.* Structural connectivity of autonomic, pain, limbic, and sensory brainstem nuclei in living humans based on 7 Tesla and 3 Tesla MRI. *Human Brain Mapping* **43**, 3086–3112 (2022).

31. Yang, W. F. *et al.* The neuroscience of highly stable, positive, and refined states of consciousness during jhana-type advanced concentration absorption meditation (ACAM-J). Preprint at <https://doi.org/10.1101/2025.11.12.688050> (2025).

32. Sorella, S., Crescentini, C., Matiz, A., Chang, M. & Grecucci, A. Resting-state BOLD temporal variability of the default mode network predicts spontaneous mind wandering, which is negatively associated with mindfulness skills. *Front. Hum. Neurosci.* **19**, 1515902 (2025).

33. Tripathi, V., Devaney, K. J., Lazar, S. W. & Somers, D. C. Silence Practice Modulates the Resting State Functional Connectivity of Language Network with Default Mode and Dorsal Attention Networks in Long-Term Meditators. *Mindfulness* **15**, 665–674 (2024).

34. Yordanova, J. *et al.* Attentional and cognitive monitoring brain networks in long-term meditators depend on meditation states and expertise. *Sci Rep* **11**, 4909 (2021).

35. Lutz, A., Dunne, J. D. & Davidson, R. J. Meditation and the neuroscience of consciousness: an introduction. in *The Cambridge Handbook of Consciousness* (eds Zelazo, P. D., Moscovitch, M. & Thompson, E.) (Cambridge University Press, 2007). doi:10.1017/CBO9780511816789.020.

36. Van Luterveld, R. *et al.* Source-space EEG neurofeedback links subjective experience with brain activity during effortless awareness meditation. *NeuroImage* **151**, 117–127 (2017).

37. Chawla, N. V., Bowyer, K. W., Hall, L. O. & Kegelmeyer, W. P. SMOTE: Synthetic Minority Over-sampling Technique. *jair* **16**, 321–357 (2002).

38. Krizhevsky, A., Sutskever, I. & Hinton, G. E. ImageNet classification with deep convolutional neural networks. *Commun. ACM* **60**, 84–90 (2017).

39. Czajko, S. *et al.* Exploring the Embodied Mind: Functional Connectome Fingerprinting of Meditation Expertise. *Biological Psychiatry Global Open Science* **4**, 100372 (2024).

40. Wilson, R. S. *et al.* Influence of epoch length on measurement of dynamic functional connectivity in wakefulness and behavioural validation in sleep. *NeuroImage* **112**, 169–179 (2015).

41. Tang, Y.-Y., Rothbart, M. K. & Posner, M. I. Neural correlates of establishing, maintaining, and switching brain states. *Trends in Cognitive Sciences* **16**, 330–337 (2012).

42. Han, C., Sun, X., Yang, Y., Che, Y. & Qin, Y. Brain Complex Network Characteristic Analysis of Fatigue during Simulated Driving Based on Electroencephalogram Signals. *Entropy* **21**, 353 (2019).

43. Zang, Y., Jiang, T., Lu, Y., He, Y. & Tian, L. Regional homogeneity approach to fMRI data analysis. *NeuroImage* **22**, 394–400 (2004).

44. Schaefer, A. *et al.* Local-Global Parcellation of the Human Cerebral Cortex from Intrinsic Functional Connectivity MRI. *Cerebral Cortex* **28**, 3095–3114 (2018).

45. Tian, Y., Margulies, D. S., Breakspear, M. & Zalesky, A. Topographic organization of the human subcortex unveiled with functional connectivity gradients. *Nat Neurosci* **23**, 1421–1432 (2020).

46. Bianciardi, M. *et al.* In vivo functional connectome of human brainstem nuclei of the ascending arousal, autonomic, and motor systems by high spatial resolution 7-Tesla fMRI. *Magn Reson Mater Phy* **29**, 451–462 (2016).

47. King, M., Hernandez-Castillo, C. R., Poldrack, R. A., Ivry, R. B. & Diedrichsen, J. Functional boundaries in the human cerebellum revealed by a multi-domain task battery. *Nat Neurosci* **22**, 1371–1378 (2019).

48. Douzas, G. & Bacao, F. Geometric SMOTE a geometrically enhanced drop-in replacement for SMOTE. *Information Sciences* **501**, 118–135 (2019).

49. Priyatno, A. M. & Widyaningtyas, T. A SYSTEMATIC LITERATURE REVIEW: RECURSIVE FEATURE ELIMINATION ALGORITHMS. *jitk* **9**, 196–207 (2024).

50. Breiman, L. Random Forests. *Machine Learning* **45**, 5–32 (2001).

51. Guyon, I., Weston, J., Barnhill, S. & Vapnik, V. Gene Selection for Cancer Classification using Support Vector Machines. *Machine Learning* **46**, 389–422 (2002).

52. Cao, L. & Shen, H. CSS : Handling imbalanced data by improved clustering with stratified sampling. *Concurrency and Computation* **34**, e6071 (2022).

53. Zhao, H. *et al.* Stratified Over-Sampling Bagging Method for Random Forests on Imbalanced Data. in *Intelligence and Security Informatics* (eds Chau, M., Wang, G. A. & Chen, H.) vol. 9650 63–72 (Springer International Publishing, Cham, 2016).

54. Freedman, D. *Statistical Models: Theory and Practice*. (Cambridge University Press, Cambridge ; New York, 2009).

55. Quinlan, J. R. Induction of decision trees. *Mach Learn* **1**, 81–106 (1986).

56. Cortes, C. & Vapnik, V. Support-Vector Networks. *Machine Learning* **20**, 273–297 (1995).

57. Cover, T. & Hart, P. Nearest neighbor pattern classification. *IEEE Trans. Inform. Theory* **13**, 21–27 (1967).

58. Rumelhart, D. E., Hinton, G. E. & Williams, R. J. Learning representations by back-propagating errors. *Nature* **323**, 533–536 (1986).

59. Chen, T. & Guestrin, C. XGBoost: A Scalable Tree Boosting System. in *Proceedings of the 22nd ACM SIGKDD International Conference on Knowledge Discovery and Data Mining* 785–794 (ACM, San Francisco California USA, 2016). doi:10.1145/2939672.2939785.

60. Friedman, J. H. Greedy function approximation: A gradient boosting machine. *Ann. Statist.* **29**, (2001).

61. McCallum, A. & Nigam, K. A Comparison of Event Models for Naive Bayes Text Classification.

62. Sutton, R. S. & Barto, A. G. Reinforcement Learning: An Introduction.

63. A study of cross-validation and bootstrap for accuracy estimation and model selection | Proceedings of the 14th international joint conference on Artificial intelligence - Volume 2. *Guide Proceedings* <https://dl.acm.org/doi/10.5555/1643031.1643047>.

64. Kubat, M., Holte, R. C. & Matwin, S. Machine Learning for the Detection of Oil Spills in Satellite Radar Images. *Machine Learning* **30**, 195–215 (1998).

65. Buda, M., Maki, A. & Mazurowski, M. A. A systematic study of the class imbalance problem in convolutional neural networks. *Neural Networks* **106**, 249–259 (2018).

66. Alberti, M., Seuret, M., Pondenkandath, V., Ingold, R. & Liwicki, M. Historical Document Image Segmentation with LDA-Initialized Deep Neural Networks. in *Proceedings of the 4th International Workshop on Historical Document Imaging and Processing* 95–100 (ACM, Kyoto Japan, 2017). doi:10.1145/3151509.3151519.

67. Dietterich, T. G. Ensemble Methods in Machine Learning. in *Multiple Classifier Systems* vol. 1857 1–15 (Springer Berlin Heidelberg, Berlin, Heidelberg, 2000).

68. Polikar, R. Ensemble based systems in decision making. *IEEE Circuits Syst. Mag.* **6**, 21–45 (2006).

69. Cohen, J. A Coefficient of Agreement for Nominal Scales. *Educational and Psychological Measurement* **20**, 37–46 (1960).

70. Pedregosa, F. *et al.* Scikit-learn: Machine Learning in Python. *MACHINE LEARNING IN PYTHON*.

71. Altmann, A., Tološi, L., Sander, O. & Lengauer, T. Permutation importance: a corrected feature importance measure. *Bioinformatics* **26**, 1340–1347 (2010).

72. Fisher, A., Rudin, C. & Dominici, F. All Models are Wrong, but Many are Useful: Learning a Variable's Importance by Studying an Entire Class of Prediction Models Simultaneously.

## Acknowledgments

We are grateful for the advanced meditators whose meditative capacities made this study possible. We also respectfully acknowledge the Buddhist traditions that have preserved and transmitted *jhana* meditation for more than two thousand years. The present study builds upon this historical knowledge by examining these advanced absorptive practices with contemporary scientific methods. Our aim here is not to uncritically validate religious claims, but rather to investigate such practices, and their outcomes, as reproducible human capacities that promise to contribute to human well-being in the modern world.

## Author Contributions

Puneet Kumar: Implementation; Formal analysis; Methodology; Writing – original draft. Winson F. Z. Yang: Data collection; Data curation; Investigation; Preprocessing; Supervision; Writing – review & editing. Alakhsimran Singh: Implementation; Results analysis; Visualization Writing – original draft. Xiaobai Li: Methodology; Supervision; Writing – review & editing. Matthew D. Sacchet: Conceptualization; Supervision; Project administration; Funding acquisition; Writing – review & editing.

## Competing interests

All authors indicate no competing interests.

## Funding

Dr. Sacchet and the Meditation Research Program are supported by the National Institute of Mental Health (Project Number R01MH125850), Dimension Giving Fund, Tan Teo Charitable Foundation, and individual donors.

## Ethics approval statement

The Mass General Brigham IRB approved the study (2019P003902) and the participants provided informed consent. The studies involving humans were approved by the Clinical Research Ethics Board. The studies were conducted in

accordance with the local legislation and institutional requirements. The participants provided their written informed consent to participate in this study

## Use of Artificial Intelligence

During manuscript preparation, the authors used ChatGPT (OpenAI) and Grammarly solely to improve language clarity. They subsequently reviewed and edited all AI-assisted text and take full responsibility for the content. No AI tools were used for data analysis, Fig. generation, or methodological design; all scientific content, results, and interpretations are the authors' own.

## Machine-Learning Implementation: Additional Details

We use ML comprehensively. This section records parameters and procedures not fully enumerated in the main manuscript to support reproduction. The visual depiction of the overall pipeline is presented in **Fig. 7** in **Section 4** of the manuscript.

### Hyper-parameters

Table 4 lists the final hyper-parameters used for the reported results (values held constant across folds unless noted).

**Table 4:** Hyper-parameter settings for various machine learning models.

Model	Hyperparameters
Logistic Regression	Regularization parameter (C) = 1.0, Penalty = 'L2'
Decision Trees	Maximum depth = 10, Criterion = 'gini'
Random Forest	Number of estimators = 100, Maximum depth = 20
Support Vector Machines (SVM)	Regularization parameter (C) = 1.0, Kernel = Linear
<i>k</i> -Nearest Neighbors (kNN)	Number of neighbors (k) = 5, Distance metric = Euclidean
Neural Networks (MLP)	Two hidden layers (sizes: 128, 64), Activation = 'ReLU', Optimizer = 'Adam', Epochs = 100

## Pseudocode

The pseudocode below summarizes the implementation details of the proposed machine learning pipeline (**Fig. 7**).

We first segment fMRI runs into planned contrasts and extract 498 ROI-level ReHo features per segment, then split data into a group-study set (for training/validation) and a case-study set (held out for the final test). Within subject-wise stratified K-folds on the group set, we (i) compute multi-view feature rankings and pre-keep the top fraction, (ii) run RFE with a validation guard to retain only informative ROIs, and (iii) address class imbalance using SMOTE on training folds only. We train several model families per fold, select the top performers by validation (e.g.,  $\kappa$ ), and form a probability-averaged ensemble. After cross-validation, we derive a global feature set, refit the top model types on the full group data, and evaluate the final ensemble once on the untouched case-study set, reporting Accuracy,  $\kappa$ , AUC, and related metrics. Finally, we aggregate feature importances across methods to generate ROI maps and, optionally, repeat the entire pipeline on revisualized features to compare against the raw analysis.

### PURPOSE

Train and evaluate binary classifiers on ROI features derived from fMRI (e.g., ReHo), while preventing data leakage, handling class imbalance, selecting informative features, finalizing an ensemble on group-study data and testing it once on a held-out case-study.

### PREP (Segmentation & Feature Extraction; done before ML)

- Segment fMRI runs into planned contrasts # e.g., ACAM-J vs control; state vs task; pairwise Jhana
- Extract 498 ROI ReHo features per segment # Schaefer-400 + Tian-32 + Bianciardi-54 + MDTB-10
- Produce two matrices:
  - `X_group, y_group, subj_ids_group` # Group study; for training/validation only
  - `X_case, y_case, subj_ids_case` # Case study; final held-out test only

### INPUTS

- `X_group : [n_group_samples × n_features]` # ROI features; group-study
- `y_group : length n_group_samples` # Binary labels
- `subj_ids_group : length n_group_samples` # Subject IDs
- `X_case : [n_case_samples × n_features]` # ROI features; case-study
- `y_case : length n_case_samples` # Binary labels; kept untouched for final test
- `subj_ids_case : length n_case_samples` # Subject IDs; for bookkeeping
- `SEED : integer` # Random seed
- `K : integer` # Cross-validation folds; subject-wise
- `FEATURE_PREKEEP_PCT : float` # e.g., 0.50 → pre-keep top 50% for RFE
- `RFE_STEP_PCT : float` # e.g., 0.05 → drop weakest 5% each step
- `RFE_MIN_FEATURES : integer` # Hard floor on number of features
- `RFE_DELTA : float` # Allowed drop below best validation score

```
MODEL_CONFIGS : dict
ENSEMBLE_TOP_L : integer
```

# Fixed hyper-parameters per model family  
# e.g., 3: average top-3 models by val metric

## OUTPUTS

```
fold_metrics : list of validation metrics across folds
selected_features_per_fold : list of feature index sets kept by RFE
trained_models_per_fold : fitted models and ensembles
final_ensemble : probability-averaged ensemble refit on FULL group-study
final_test_metrics : metrics on held-out case-study
Spec, p-value
S_agg_importance : aggregated feature-importance vector (normalized [0,1]) for ROI maps
```

# Accuracy, Kappa, AUC, etc.  
# One per fold  
# Acc, Kappa, AUC, Prec, Rec, F1, Sens,

## SETUP

```
set_global_random_seed(SEED)
define subject-wise, stratified K-fold splits on (X_group, y_group, subj_ids_group) so that:
- no subject appears in both train and validation within the same fold
- class proportions are preserved per fold
```

## OPTIONAL STEP 0 : Prior-driven ROI pre-filter (if used)

```
P ← prior_based_roi_mask
restrict X_group and X_case to columns P (downstream steps operate within P)
```

## CROSS-VALIDATION LOOP (on GROUP-STUDY only)

for each fold in K folds:

```
(X_train, y_train, X_val, y_val) ← split_by_subject(subj_ids_group, X_group, y_group, fold_index)
```

-----  
STEP 1 — Feature Ranking (quick screening before RFE; TRAIN ONLY)

```
rf_score ← RandomForest_importance(X_train, y_train, MODEL_CONFIGS["RF"])
lin_score ← abs(LinearModel_coefficients(X_train, y_train, MODEL_CONFIGS["LR_or_SVM"]))
mi_score ← MutualInformation(X_train, y_train)

rf_rank ← normalize_to_rank_percentile(rf_score)
lin_rank ← normalize_to_rank_percentile(lin_score)
mi_rank ← normalize_to_rank_percentile(mi_score)

consensus_rank ← (rf_rank + lin_rank + mi_rank) / 3
C ← keep_lowest_fraction(consensus_rank, FEATURE_PREKEEP_PCT)    # e.g., Top 50%
```

-----  
STEP 2 — RFE (Recursive Feature Elimination) with validation guard

---

```

F_current ← C
best_score ← -∞
F_best ← F_current

while size(F_current) > RFE_MIN_FEATURES:
    RF ← fit_RandomForest(X_train[:, F_current], y_train, MODEL_CONFIGS["RF"])
    val_score ← evaluate_metric(RF, X_val[:, F_current], y_val)

    if val_score < (best_score - RFE_DELTA):                      # Early stop if degradation exceeds δ
        break

    if val_score > best_score:
        best_score ← val_score
        F_best ← copy(F_current)

    importances ← RF.feature_importances_
    weakest ← indices_of_lowest_fraction(importances, RFE_STEP_PCT)      # e.g., Bottom 5%
    F_current ← remove_indices(F_current, weakest)

F_final ← F_best
selected_features_per_fold.append(F_final)

```

---

#### STEP 3 — Class Imbalance Handling (TRAIN ONLY)

---

```

(X_train_bal, y_train_bal) ← SMOTE_resample(
    X_train[:, F_final], y_train,
    k_neighbors=5, random_state=SEED, sampling_strategy="auto" )

```

---

#### STEP 4 — Model Training and Fold Ensemble

---

```

trained_models ← {}
for model_name in ["LR", "DT", "RF", "SVM", "KNN", "MLP"]:
    model ← fit_model(model_name, X_train_bal, y_train_bal, MODEL_CONFIGS[model_name])
    trained_models[model_name] ← model

top_models ← select_top_by_validation(
    trained_models, X_val[:, F_final], y_val, metric="Kappa", L=ENSEMBLE_TOP_L)
ensemble ← probability_average(top_models)                      # Threshold 0.5
trained_models_per_fold.append({"models": trained_models, "ensemble": ensemble})

```

## STEP 5 — Validation Evaluation (no augmentation)

```
y_pred ← predict_with(ensemble, X_val[:, F_final])
fold_metrics.append(compute_metrics(y_val, y_pred))
```

# Acc, Kappa, AUC, Prec, Rec, F1, etc.

END LOOP

## POST-CV — Derive a Global Feature Set and Refit on FULL GROUP-STUDY

```
F_final_global ← union_or_consensus(selected_features_per_fold)
```

# e.g., Intersection/majority vote/mean-rank

```
Xg, yg ← (X_group[:, F_final_global], y_group)
```

```
Xg_bal, yg_bal ← SMOTE_resample(Xg, yg, k_neighbors=5, random_state=SEED, sampling_strategy="auto")
```

```
models_full ← {}
```

```
for model_name in ["LR", "DT", "RF", "SVM", "KNN", "MLP"]:
```

```
models_full[model_name] ← fit_model(model_name, Xg_bal, yg_bal, MODEL_CONFIGS[model_name])
```

```
top_models_full ← select_top_by_cv_summary(models_full, fold_metrics, metric="Kappa", L=ENSEMBLE_TOP_L)
```

```
final_ensemble ← probability_average(top_models_full)
```

## FINAL HELD-OUT TEST — CASE-STUDY (UNMODIFIED)

```
ŷ_case ← predict_with(final_ensemble, X_case[:, F_final_global])
```

```
final_test_metrics ← compute_metrics(y_case, ŷ_case)
```

# Acc, Kappa, AUC, Prec, Rec, F1, Sens, Spec

```
p_values ← permutation_test(
```

```
evaluation_metric, X_group, y_group, subj_ids_group, K,
iterations=1000, seed=SEED, subject_wise=True, right_tailed=True,
test_on=(X_case[:, F_final_global], y_case)
```

```
)
```

## FEATURE-IMPORTANCE AGGREGATION (for maps; normalized to [0,1])

```
S_rf ← normalize_0_1(RandomForest_importance on (Xg_bal, yg_bal) using F_final_global)
```

```
S_lin ← normalize_0_1(abs(Linear/Linear-SVM coefficients on (Xg_bal, yg_bal)))
```

```
S_perm ← normalize_0_1(PermutationImportance(final_ensemble, Xg_bal, yg_bal))
```

```
S_agg_importance ← mean({S_rf, S_lin, S_perm})
```

# project to ROIs for brain maps/overlaps

## OPTIONAL

# Residualization Rerun

```
X_group_resid ← regress_out(phenomenology/trait covariates from X_group)
```

# Train-only fits inside CV

```
X_case_resid ← apply_residual_transform(X_case)
```

# Parameters from group train folds

```
repeat full pipeline with (X_group_resid, y_group, subj_ids_group) → test on X_case_resid
```

```
compare (final_test_metrics_resid vs final_test_metrics_raw)
```

RETURN

```
fold_metrics, selected_features_per_fold, trained_models_per_fold,
final_ensemble, final_test_metrics, p_values (if computed), S_agg_importance
```

### SMOTE Implementation Details for class Imbalance handling

Class balancing is performed only on training data within each subject-wise fold of the group-study set, never on validation or the held-out case-study. For each segment/contrast, we target a fixed representation of 27 runs per segment to stabilize model fitting. Within a segment, we treat the run identifier as a temporary class label and apply SMOTE to the numeric ROI feature matrix, thereby synthesizing samples that interpolate between nearest neighbors in feature space. The neighbor count is chosen dynamically as ‘`k_neighbors = min(5, min_class_size-1)`’, where ‘`min_class_size`’ is the smallest run frequency in the current training fold; this guards against overfitting when some runs are scarce. If a segment is degenerate (single run class or ‘`min_class_size ≤ 1`’), we first create minimal pseudo-classes by duplication/relabeling; if SMOTE remains infeasible, we fall back to controlled replication with noise. Post-SMOTE (or replication), we apply a light perturbation to numeric columns, Gaussian noise scaled by column SD with ‘`noise_level = 0.05`’, blended as ‘ $x = 0.5 \cdot x + 0.5 \cdot \text{noise}$ ’ (‘`retention_degree`’ = 0.5), modifying around 80% of numeric columns per pass (‘`interpolation_proportion = 0.8`’). All stochastic steps use ‘`random_state = 42`’. The augmented set is then trimmed or extended to exactly 27 runs per segment, with fresh sequential run labels to keep uniqueness within (subject, segment).

Operationally, the sequence per fold is: split by subject → feature selection (ranking → RFE) on train only → SMOTE/augmentation on the selected-feature matrix of the train fold → model training → validation on untouched data; after cross-validation, we recompute a global feature set, repeat the same SMOTE/augmentation on the full group-study subset, fit the final ensemble, and evaluate once on the untouched case-study. These settings correspond to the “SMOTE & balancing” phase in **Fig. 7** and the fold-safe training order are provided here so that an independent reader can replicate the balancing behavior byte-for-byte.

## Extended Results

### Ensemble Method and Model Appearance Statistics

For each of the 19 binary pairs (e.g., J1 vs J2, J2 vs J3, J vs Control), we trained all six model families shown in **Fig. 7** (LR, DT, RF, SVM-linear, kNN, MLP) under the fold-safe protocol. Per pair, we ranked models by validation Cohen’s  $\kappa$  (ties broken by higher AUC), selected the top three, and formed an ensemble by probability averaging of

their predicted class probabilities (threshold 0.5 unless otherwise stated). Across all pairs, this yields 57 model slots (19 pairs  $\times$  top 3 per pair). The count of how often each family appeared in the top 3 is:

- $k$ -Nearest Neighbors: 13/57 (22.8%)
- Logistic Regression: 12/57 (21.1%)
- Neural Network (MLP): 11/57 (19.3%)
- SVM (linear): 8/57 (14.0%)
- Decision Tree: 7/57 (12.3%)
- Random Forest: 6/57 (10.5%)

These frequencies summarize which inductive biases most often contributed to the final ensembles across contrasts; the ensemble itself is always the probability average of the per-pair top 3 models selected by validation  $\kappa$ .

### Computational timing

All runs were executed end-to-end for the 19 pairs on a machine with 10-core CPU, NVIDIA V100 GPU, 256 GB RAM, and  $n_{\text{jobs}} = -1$  where applicable. The total wall-clock time for the ML pipeline (feature ranking  $\rightarrow$  RFE  $\rightarrow$  SMOTE on training folds  $\rightarrow$  per-pair model training/selection  $\rightarrow$  ensemble formation  $\rightarrow$  final case-study inference) was 11,734.62 s ( $\approx 3$  h 15 m 35 s). Timings may vary with fold seeds, library versions, and I/O, but this Fig. provides a reproducible order-of-magnitude reference for the configuration reported here.